Nano Research 2017, 10(8): 2772–2781
DOI 10.1007/s12274-017-1481-y
Research Article
ISSN 1998-0124
CN 11-5974/O4

Ultrahigh quantum efficiency photodetector and ultrafast reversible surface wettability transition of square In_2O_3 nanowires

Ming Meng[1,2], Xinglong Wu[2] (✉), Xiaoli Ji[3], Zhixing Gan[4], Lizhe Liu[2], Jiancang Shen[2], and Paul K. Chu[5]

[1] *School of Physics and Telecommunication Engineering, Zhoukou Normal University, Zhoukou 466001, China*
[2] *Key Laboratory of Modern Acoustics, MOE, Institute of Acoustics, Collaborative Innovation Center of Advanced Microstructures, National Laboratory of Solid State Microstructures, Nanjing University, Nanjing 210093, China*
[3] *School of Electronic Science and Engineering, Nanjing University, Nanjing 210093, China*
[4] *Key Laboratory of Optoelectronic Technology of Jiangsu Province, School of Physical Science and Technology, Nanjing Normal University, Nanjing 210023, China*
[5] *Department of Physics and Materials Science, City University of Hong Kong, Tat Chee Avenue, Kowloon, Hong Kong, China*

Received: 28 October 2016
Revised: 1 January 2017
Accepted: 14 January 2017

KEYWORDS

square In_2O_3 nanowires, crystal facet, photodetector, reversible wettability transition

ABSTRACT

Due to a large surface-to-volume ratio, the optoelectronic performance of low-dimensional semiconductor nanostructure-based photodetectors depends in principle on chemisorption/photodesorption at the exposed surface, but practical examples that show such an effect are still unavailable. Some theoretical calculations have predicted that the {001} facets of In_2O_3 can effectively accumulate photogenerated holes under irradiation, providing a model material to examine whether the facet cutting of nanowires (NWs) can boost their optoelectronic performance. Herein, we present the design and construction of a novel nanowire-based photodetector using square In_2O_3 NWs with four exposed {001} crystal facets. The photodetector delivers excellent optoelectronic performance with excellent repeatability, fast response speed, high spectral responsivity (R_λ), and high external quantum efficiency (EQE). The R_λ and EQE values are as high as 4.8×10^6 A/W and 1.46×10^9%, respectively, which are larger than those of other popular semiconductor photodetectors. In addition, the square In_2O_3 NWs show hydrophobic wettability as manifested by a contact angle of 118° and a fast photoinduced reversible switching behavior is observed.

1 Introduction

Low-dimensional semiconductor nanostructures have attracted considerable attention since they provide possibilities for revolutionary advances in nanodevices such as photodetectors, photovoltaics, and lasers [1–4].

Address correspondence to hkxlwu@nju.edu.cn

In particular, nanostructured photodetectors have promising applications in light-wave communication, optical imaging, optoelectronic integrated circuits, and so on [5–8]. As such, considerable effort has been put into designing and fabricating photodetectors using different kinds of nanostructures [9–15]. Nevertheless, owing to the large surface-to-volume ratio and abundant surface states, photogenerated carriers can be lost due to surface recombination, thereby shortening the carrier lifetime and compromising the performance of the nanophotodetector [16, 17]. To solve this problem, several strategies have been proposed, for instance, surface modification (such as surface passivation, metal deposition) and fabrication of heterostructures [16, 18, 19]. Despite recent advances, the performance of photodetectors still cannot meet practical demand and a novel approach to suppress surface recombination of photogenerated carriers is imperative. It has recently been shown that photogenerated electrons and holes can be driven to different crystal facets by the difference in the energy levels between the facets to promote separation of the photogenerated carriers [20–23]. This phenomenon may be exploited to enhance the optoelectronic properties of nanostructures by controlling the exposed facets.

Indium oxide (In_2O_3), an important n-type semiconductor with excellent electrical and optical properties, is a prospective building block for next-generation electronic and optoelectronic devices [24–28]. Theoretical calculation has predicted that the polar {001} facets of In_2O_3 can accumulate photogenerated holes [29–31], implying that the optoelectronic performance can be boosted by chemisorption/photodesorption of oxygen. Hence, a photodetector composed of a single In_2O_3 nanowire (NW) with only the exposed {001} facet may deliver enhanced optoelectronic performance. The operating principle of a single In_2O_3 NW-based photodetector is displayed in Figs. 1(a) and 1(b). Under dark conditions, oxygen molecules tend to chemisorb onto the n-type In_2O_3 NW {001} facets by trapping free electrons from the conduction band and becoming negative ions O_2^-, which reduces the free electron density, $O_2^-(g) + e^- \rightarrow O_2^-(ad)$. This process forms a depletion layer and upward surface band bending (SBB) near the {001} facets leading to low conductivity. When illuminated with light energy above the bandgap of In_2O_3, electron–hole pairs are created in the bulk. Owing to the presence of new valence subbands, the photogenerated holes will migrate from the bulk towards the top exposed {001} facets and these accumulated holes can react with the negatively charged adsorbed oxygen ions, resulting in oxygen desorption and concomitant release of the captured free electron $h^+ + O_2^-(ad) \rightarrow O_2(g)$. Oxygen desorption can reduce the SBB and decrease the width of the depletion layer, so that the square In_2O_3 NW delivers better optoelectronic performance than other nanostructures. Furthermore, it is found that the square In_2O_3 NWs also show a faster transition of the photoinduced surface wettability between hydrophobicity and hydrophilicity as a result of the unique surface electronic band structure.

2 Experimental

2.1 Sample preparation

In_2O_3 NWs were fabricated by chemical vapor deposition (CVD) [31]. A mixture of high-purity In_2O_3 (0.2 g, 99.99%) and active carbon (0.3 g) was used as the source and loaded onto an alumina boat which was inserted into a quartz tube at the front end of a furnace. A Si wafer (0.5 mm thick, and 1 cm × 1 cm in size) coated with a 5 nm thick gold film was placed downstream in the quartz tube to collect the products. Prior to heating, the furnace was evacuated to 20 mTorr to remove residual oxygen from the system. The furnace was heated to 1,100 ˚C in 20 min and kept at this temperature for 2.5 h. During sample fabrication, a mixture of Ar (98%) and O_2 (2%) was bled at a flow rate of 100 sccm and the pressure inside the furnace was 1 atm. After the system was cooled to room temperature, a light grey layer was deposited on the silicon substrate.

2.2 Fabrication of field-effect transistors (FETs) and photodetectors

To fabricate the single-NW-based devices, the In_2O_3 NW was carefully detached from the Si substrate by ultrasonic treatment to produce a suspension in ethanol with a density ensuring successful preparation of a single NW device. The NWs were dispersed in low

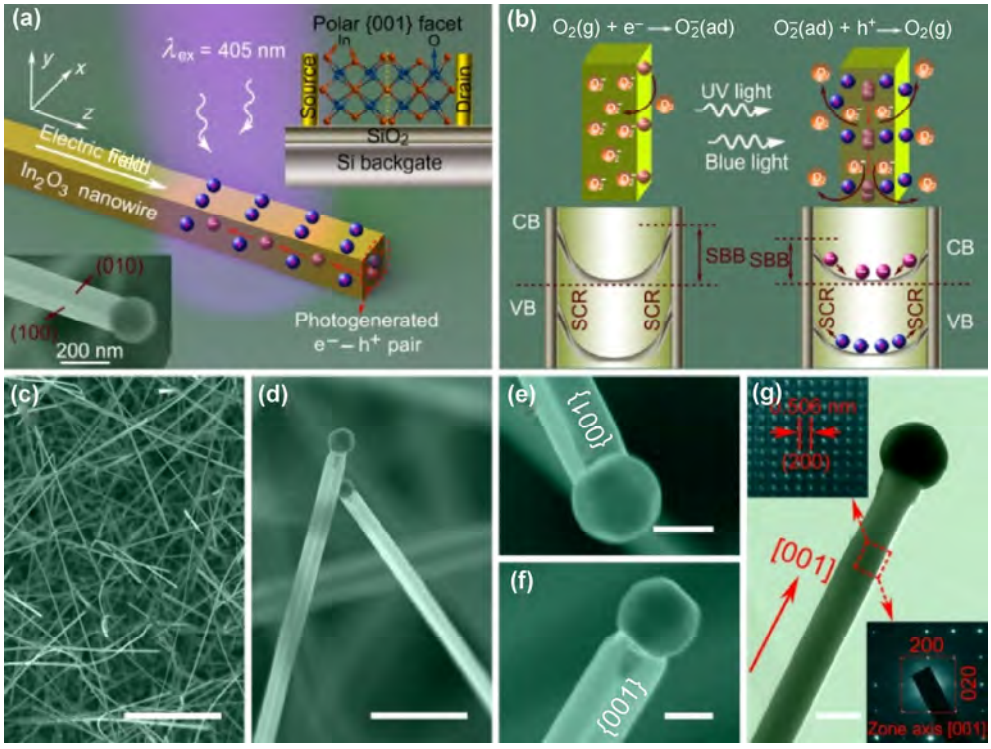

Figure 1 (a) Operating principle of the photodetector comprising a single In_2O_3 NW. (b) Corresponding schematic showing SBB caused by oxygen chemisorption/photodesorption with and without light illumination. (c) and (d) Low- and high-magnification FE-SEM images of the In_2O_3 NWs. (e) and (f) High-magnification FE-SEM images acquired from different directions of a NW showing the square cross section. (g) Low-magnification image of a single In_2O_3 NW. The top left and bottom right insets depict the HR-TEM image and SAED pattern of the area marked by the red dashed box. Scale bars: (c) 10 and (d) 1 μm, and (e)–(g) 100 nm.

densities onto 300 nm SiO_2/Si substrates by spin casting. The SiO_2/Si substrates were first subject to a 30 min UV/ozone treatment, followed by spinning at 1,000 rpm. Standard photolithography was employed to pattern the electrodes of In_2O_3 back-gated FETs onto the 300 nm SiO_2/Si substrates. Ti/Au (10/100 nm) source and drain electrodes were deposited on top of the NWs by electron-beam deposition, followed by lift-off. All devices were annealed at 300 °C in Ar to improve contacts.

2.3 Characterization

The In_2O_3 NWs were characterized by X-ray powder diffraction (XRD, Philips, Xpert), field-emission scanning electron microscopy (FE-SEM, Hitachi S4800), high-resolution transmission electron microscopy (HR-TEM, JEOL-2100), X-ray photoelectron spectroscopy (XPS, PHI5000 VersaProbe), and a VARIAN Cary 5000 spectrophotometer. The electronic and optoelectronic measurements were conducted on the Keithley 4200 semiconductor characterization system in a Cascade Summit 12000 probe station. In the photoresponse determination, 350, 405, 470, 505 and 625 nm laser diodes were employed. All the measurements were all performed in air and at room temperature unless mentioned otherwise. The surface wettability was evaluated by measuring the water contact angle (CA) using an OCA200 contact angle system (Dataphysics, Germany).

3 Results and discussion

3.1 Structural characterization

The XRD results in Fig. S1 in the Electronic Supplementary Material (ESM) show strong, sharp reflection peaks that can be indexed to the body-centered cubic (bcc) structure of In_2O_3 (JCPDS card No. 06-0416), suggesting that the In_2O_3 NWs have high crystallinity. No impurity peaks are observed. The XPS spectra

provide evidence of the formation of pure In_2O_3 with some oxygen deficiencies (Fig. S2 in the ESM). FE-SEM images show that the product consists of a large quantity of NWs with lengths ranging from several tens to hundreds of micrometers and a uniform width over their entire length (Fig. 1(c) and Figs. S3(a) and S3(b) in the ESM). Figure 1(d) and Fig. S3(c) in the ESM show that the square In_2O_3 NWs have a uniform size distribution and the average width is approximately 100 nm. Hence, the square In_2O_3 NWs can be used to construct a single NW-based photodetector with excellent repeatability and stability. The high-magnification FE-SEM images of an individual In_2O_3 NW obtained from different directions (Figs. 1(e) and 1(f), and Fig. S4(a) in the ESM) show that the NW has typical rectangular prismatic morphology with four smooth lateral facets between adjoining edges with corresponding interfacial angles of 90°. This value is identical to the theoretical value for the angle between the {100} and {010} facets of the bcc structure of In_2O_3 (Figs. S4(b) and S4(c) in the ESM). FE-TEM was performed to identify the crystallographic growth direction and exposed lateral facets of the square NWs. The low-magnification FE-TEM image in Fig. 1(g) confirms the wire-like geometry and the HR-TEM image reveals {200} and {020} crystallographic facets with a lattice spacing of 0.506 nm and interfacial angle of 90°, implying that the preferred growth direction of the square In_2O_3 NWs is along the {001} orientation (top left inset in Fig. 1(g) and Fig. S4(d) in the ESM). The selected area electron diffraction (SAED) pattern displays a square diffraction spot (bottom right inset in Fig. 1(g)). These results provide convincing evidence that each square In_2O_3 NW is enclosed by four high-symmetry {001} facets. The growth mechanism has been described in our previous work [31]. Succinctly speaking, a combination of both Au catalytic vapor–liquid–solid (VLS) and vapor–solid (VS) mechanisms is responsible for formation of square In_2O_3 NWs.

3.2 Optoelectronic performance of a single In_2O_3 NW

Photodetectors based on a single In_2O_3 NW were fabricated and their optoelectronic properties were determined. A schematic of the single NW-based photodetector and representative FE-SEM image are

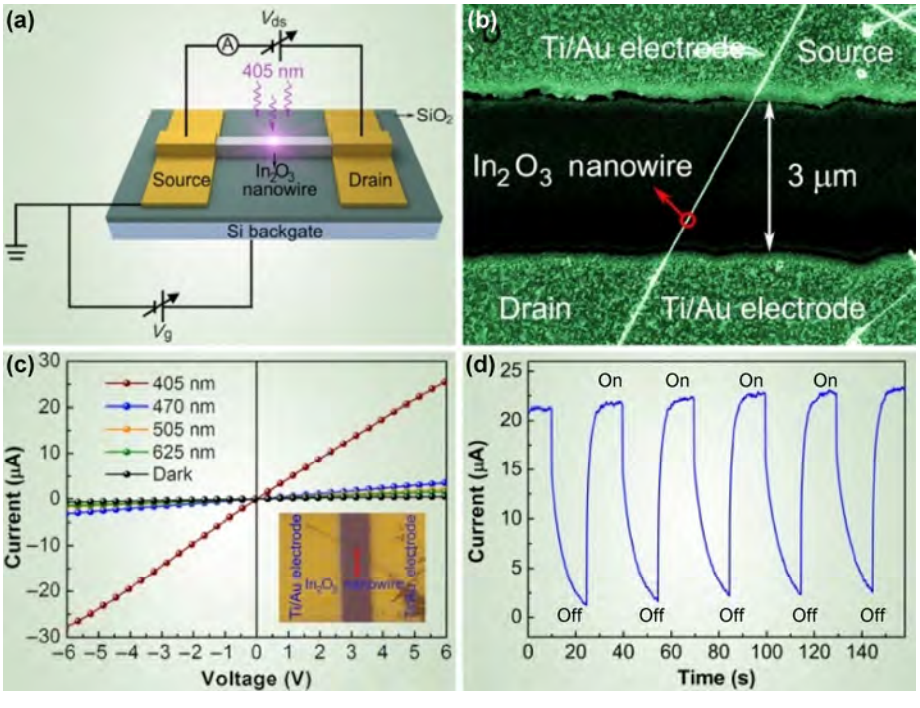

Figure 2 (a) and (b) Schematic and FE-SEM image of a single In_2O_3 NW-based photodetector structure. (c) *I*–*V* curves of the NW-based photodetector with and without light illumination at different wavelengths. The inset shows a micrograph of the device. (d) Current–time response measured by periodically switching on and off 405 nm light illumination at a bias of 5 V.

presented in Fig. 2(a) and 2(b), respectively. As shown in Fig. 2(a), two Ti/Au electrodes (10 nm/100 nm) with a 3 μm separation are deposited onto the In_2O_3 NWs on the SiO_2/Si substrate, which serve as the source and drain, respectively. The NW connecting the two electrodes has a typical length of 3.7 μm and width of 100 nm and is exposed to light as shown in Fig. 2(b) (denoted as device 1). The inset of Fig. 2(c) and Fig. S5 in the ESM show typical optical images of the device. A clear contrast is visible between the NW and Au electrode on the SiO_2/Si substrate, corroborating the FE-SEM result in Fig. 2(b) and demonstrating that there is only one NW between source and drain. The current versus voltage (*I*–*V*) curves of device 1, measured with and without light exposure at different wavelengths, are displayed in Fig. 2(c) and Fig. S6 in the ESM. The linear and symmetrical *I*–*V* curves suggest good Ohmic contact between the NW and Ti/Au electrodes [32]. The electrical transport characteristics of the NW measured based on the back-gated In_2O_3 NW FETs as shown in Fig. S7 in the ESM also confirm this point [24–26]. The dark current of the device is 0.45 μA. Under illumination with light wavelengths of 470 nm (0.79 mW/cm^2), 505 nm (0.55 mW/cm^2), and 625 nm (0.46 mW/cm^2), the photocurrents slightly increase compared to the dark current. In contrast, when exposed to light energy greater than the bandgap of In_2O_3 (2.8 eV, 442 nm), the photocurrents increase drastically. To demonstrate this phenomenon more clearly, the photocurrent measured at 5 V is shown in Fig. S8 in the ESM. When illuminated with 405 nm light (1.21 mW/cm^2), the photocurrent reaches 21.7 μA which indicates a 47-fold enhancement compared to that in darkness. The results demonstrate the excellent photoresponse ability and wavelength selectivity of the square NW-based photodetector.

Generally, the repeatability and response speed are key parameters of a photodetector [33]. To evaluate these two factors, the current–time response was examined by periodically switching on and off the 405 nm light illumination in air at a bias of 5 V (Fig. 2(d) and Fig. S9(a) in the ESM). When the light is turned on, the photocurrent increases rapidly to a stable value of 21.7 μA and then sharply reverts to the original value when the light is turned off. The reversible periodic switching between on and off states upon turning on/off light illumination is clearly observed during the entire observation time of 10 min, which suggests excellent repeatability and stability. The rise and decay times, defined as the time needed for peak photocurrent to change from 10% to 90% of its maximum value or vice versa [9], were measured to be 3 and 13 s, respectively. In addition, they are stable after 20 switching cycles and much faster than the values previously observed from In_2O_3-based photodetectors as shown in Fig. S9(b) and Tables S1 and S2 in the ESM [27, 34].

In addition to the repeatability and response rate, the spectral responsivity (R_λ) and external quantum efficiency (EQE) or quantum efficiency (QE) are two important parameters for a photodetector and they impact applications [12, 35]. R_λ can reflect the wavelength selectivity of a photodetector and is defined as the ratio of the photocurrent to the incident light intensity. EQE is related to the sensitivity and is defined as the conversion rate of photons to electron–hole pairs. They can be expressed by the following equations, respectively

$$R_\lambda = \frac{\Delta I}{PS} \quad (1)$$

$$\mathrm{EQE} = \frac{hc}{e\lambda} R_\lambda \quad (2)$$

Where ΔI is the difference between the photocurrent and dark current, P is the incident light power density, S is the effective illumination area of the photodetector, h is Planck's constant, c is the speed of light, e is the electronic charge, and λ is the wavelength of the incident light. Based on Fig. S8 in the ESM, R_λ and EQE of the NW-based photodetector can be calculated and the results are shown in Fig. 3(a). When irradiated with 405 nm light, the R_λ and EQE values are as large as 4.8×10^6 A/W and 1.46×10^9% at an applied voltage of 5 V. Both values are not only the largest among the reported In_2O_3-based photodetectors, but also larger than those of many other popular semiconductor photodetectors as shown in Table S3 in the ESM [36]. More importantly, R_λ and EQE values remain almost unchanged after 20 switching cycles, providing more evidence for the stability of the NW-based photodetector (Fig. S10 and Table S1 in the ESM).

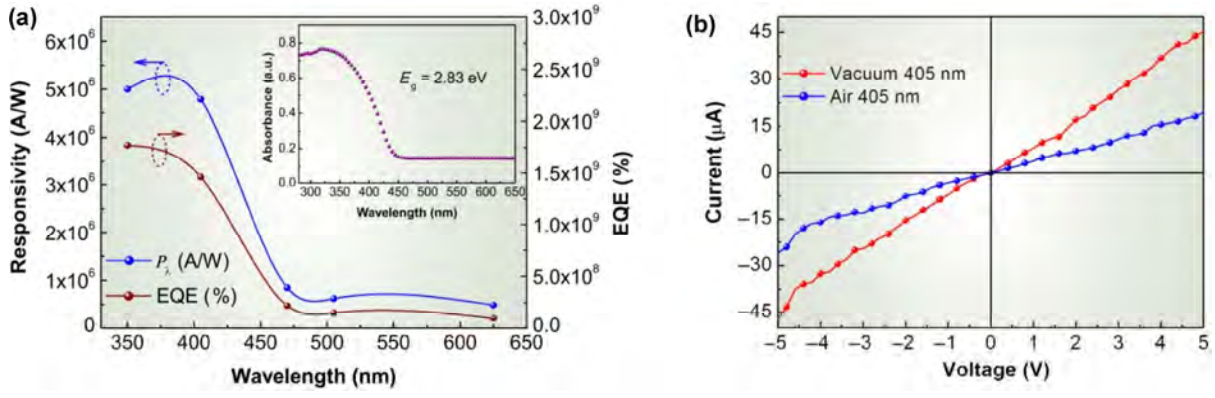

Figure 3 (a) Responsivity and EQE versus incident wavelength at a bias of 5 V. (b) *I*–*V* curves of the NW-based photodetector illuminated with light of 405 nm in air and under vacuum conditions.

Such an ultrahigh EQE may be attributed to the exposure of {001} facets via chemisorption/photodesorption of oxygen. As mentioned above, due to the presence of new valence subbands, under illumination more photogenerated holes can accumulate on the {001} facets and discharge the negatively charged adsorbed oxygen ions, resulting in oxygen desorption and concomitant release of the captured free electron. The *I*–*V* characteristics of device 1 in a vacuum and air were further investigated as shown in Fig. 3(b) and Fig. S11 in the ESM. The dark current measured under vacuum conditions is about 1.6 times larger than that in air at an applied voltage of 5 V, verifying the existence of oxygen chemisorption/photodesorption on the {001} facets [12, 13]. The photocurrent obtained under vacuum conditions is about 2.3 times larger than that in air, which reveals that the exposed {001} facets play a crucial role in the enhanced optoelectronic performance. This justifies the use of In_2O_3 NWs with exposed {001} facets as the building blocks of photodetectors. Additionally, when the wavelength of the incident light was changed, R_λ exhibited an obvious dependence on the wavelength. It is evident that R_λ is very low for wavelengths longer than 470 nm and start to gradually increase when illuminated by light with energy above the bandgap of In_2O_3, confirming the wavelength selectivity. This is consistent with the stronger absorption at wavelengths below 442 nm in the UV–vis absorption spectrum (inset in Fig. 3(a)). The high spectral selectivity and large EQE suggest that the square In_2O_3 NWs have great potential for use in blue/UV-light photodetectors (below 442 nm).

To study the reproducibility of the photosensitive properties of the In_2O_3 NWs, 20 photodetectors were prepared by the same procedure. The insets of Figs. S12(a) and S12(b) in the ESM depict the typical FE-SEM images of two devices (denoted as devices 2 and 3) with different channel widths between two electrodes. The corresponding *I*–*V* curves obtained under the same conditions reveal that they have the same trend as the shown device above, suggesting good reproducibility. The slight difference in the photocurrent is ascribed to the difference in the effective illumination area between these two devices.

3.3 Reversible wettability switching behavior of square In_2O_3 NWs

The square In_2O_3 NWs not only deliver high performance as a photodetector, but also show controllable wettability including fast conversion between hydrophobic and hydrophilic states. Smart devices such as intelligent microfluidic switches have attracted attention and functional surfaces with reversible and tunable wettability are of interest [37–40]. The surface wettability of the square In_2O_3 NWs was assessed by measuring the CA and the results are shown in Fig. 4 and Fig. S13 in the ESM. The water CA on the square In_2O_3 NWs was about 118° (Fig. 4(a)), nearly 6 times larger than that of pure In_2O_3 film and comparable to those of multikinked and ultrathin In_2O_3 NWs

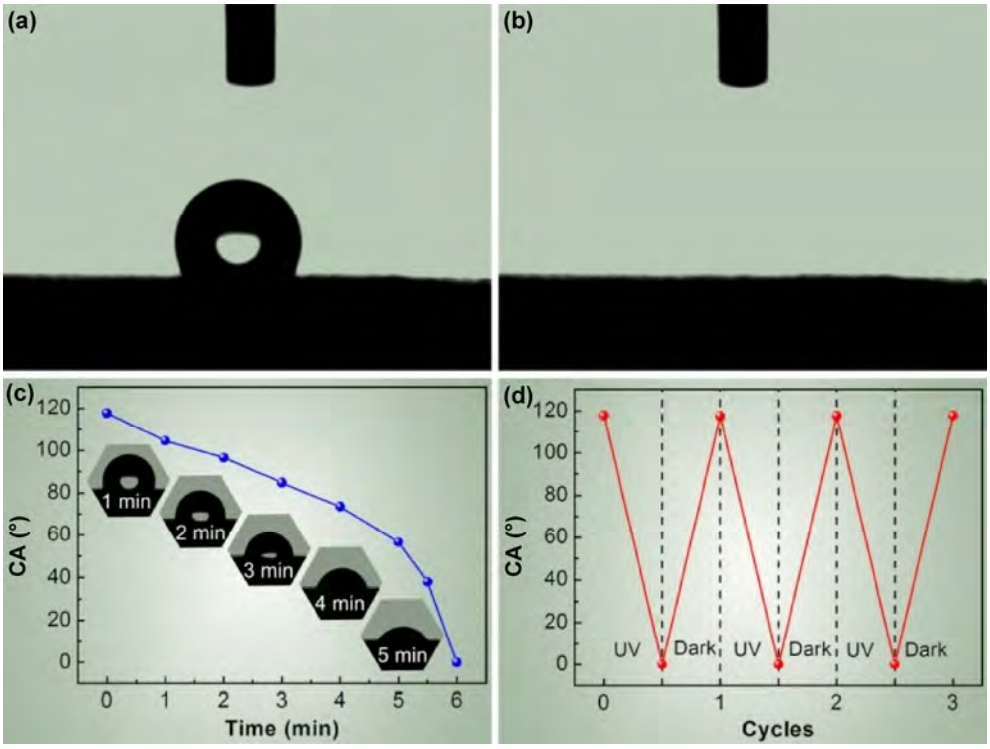

Figure 4 Reversible photoinduced wettability transition on the squared In_2O_3 NWs tested with a water droplet: (a) before and (b) after UV illumination. (c) Water contact angles as a function of UV illumination time. The optical images display gradual decrease in the water contact angles under UV illumination. (d) Reversible wettability transition by alternating UV illumination and dark storage.

[24, 25, 41]. As reported, the air trapped in the troughs between randomly distributed In_2O_3 NWs is responsible for their hydrophobic nature [42].

The evolution of the CA on the square In_2O_3 NWs with UV light (30 W, 365 nm) exposure time is illustrated in Fig. 4(c). The CA gradually decreases with exposure time as shown in the inset in Fig. 4(c), in which the sequence of spreading water droplets on the surface under UV irradtion is revealed. After exposure to UV light for 6 min, the CA of the square In_2O_3 NWs was about 0° (Fig. 4(b)), indicative of switching from the hydrophobic to hydrophilic states. Upon UV irradiation, electrons and holes are generated in the conduction band (CB) and valence band (VB) of the square In_2O_3 NWs, respectively. The photogenerated holes tend to transfer to the {001} facets first and then oxidize the lattice oxygen to produce surface oxygen vacancies, that is, surface defective sites. It has been demonstrated that such defective sites can enhance H_2O dissociative adsorption on account of strong adsorption between oxygen vacancies and hydroxyl groups, thereby making the surface of the square In_2O_3 NWs hydrophilic [43, 44]. The hydrophobic/ hydrophilic transition rate of the square In_2O_3 NWs was 19.6 °/min, which is about 50 times that of the aligned In_2O_3 NWs arrays (0.4 °/min) and much faster than the transition rate of 13.4 °/min observed from ultrathin In_2O_3 NWs before [24]. This may be ascribed to the exposed {001} facets ability to effectively gather photogenerated holes. When irradiated with UV light, more photogenerated holes accumulate on the {001} facets leading to the formation of more oxygen vacancies on the surface. Consequently, it is not surprising that the square In_2O_3 NWs exhibit a faster hydrophobicity–hydrophilicity transition rate. When the UV irradiated In_2O_3 NWs are stored in darkness for 1 week, the wettability reverts to the native hydrophobic state and the process can be repeated (Fig. 4(d)). This reversible wettability is believed to arise from replacement of hydroxyl adsorption on the surface defective sites by oxygen in air and darkness because oxygen adsorption is thermodynamically more stable, thereby returning the surface of square In_2O_3 NWs to their native state.

4 Conclusions

In summary, a novel NW-based photodetector was designed and constructed with square In_2O_3 NWs with exposed four {001} facets. The photodetector delivers excellent optoelectronic performance including excellent repeatability, fast response speed, high spectral responsivity, and external quantum efficiency. The R_λ and EQE values were as high as 4.8×10^6 A/W and 1.46×10^9%, respectively, which are larger than those of other popular semiconductor photodetectors. In addition, the square In_2O_3 NWs showed hydrophobic wettability as manifested by a CA of 118° and a fast photoinduced reversible switching behavior was observed.

Acknowledgements

This work was supported by the National Basic Research Program of China (Nos. 2014CB339800 and 2013CB932901) and National Natural Science Foundation of China (Nos. 11374141, 61264008, 21203098 and 21375067). Partial support was provided by City University of Hong Kong Applied Research Grant (ARG) (No. 9667122).

Electronic Supplementary Material: Supplementary material (Table S1: key parameters of photodetector after 20 periodic change; Tables S2 and S3: comparison of some characteristic parameters from this work and previous reports; Figs. S1–S5: XRD pattern, XPS spectra, SEM, schematic model and optical images of square In_2O_3 NWs; Figs. S6–S11: *I–V*, *I–t* and I_{ds}–V_{ds} curves of device 1; Fig. S12: SEM images, *I–V* curves of devices 2 and 3; Fig. S13: contact angles measured from different In_2O_3 samples) is available in the online version of this article at https://doi.org/10.1007/s12274-017-1481-y.

References

[1] Youngblood, N.; Chen, C.; Koester, S. J.; Li, M. Waveguide-integrated black phosphorus photodetector with high responsivity and low dark current. *Nat. Photonics* **2015**, *9*, 247–252.

[2] Chen, H. Y.; Liu, H.; Zhang, Z. M.; Hu, K.; Fang, X. S. Nanostructured photodetectors: From ultraviolet to terahertz. *Adv. Mater.* **2016**, *28*, 403–433.

[3] Tang, J. Y.; Huo, Z. Y.; Brittman, S.; Gao, H. W.; Yang, P. D. Solution-processed core–shell nanowires for efficient photovoltaic cells. *Nat. Nanotechnol.* **2011**, *6*, 568–572.

[4] Oulton, R. F.; Sorger, V. J.; Zentgraf, T.; Ma, R. M.; Gladden, C.; Dai, L.; Bartal, G.; Zhang, X. Plasmon lasers at deep subwavelength scale. *Nature* **2009**, *461*, 629–632.

[5] Assefa, S.; Xia, F. N.; Vlasov, Y. A. Reinventing germanium avalanche photodetector for nanophotonic on-chip optical interconnects. *Nature* **2010**, *464*, 80–84.

[6] Takahashi, T.; Yu, Z. B.; Chen, K.; Kiriya, D.; Wang, C.; Takei, K.; Shiraki, H.; Chen, T.; Ma, B. W.; Javey, A. Carbon nanotube active-matrix backplanes for mechanically flexible visible light and X-ray imagers. *Nano Lett.* **2013**, *13*, 5425–5430.

[7] Keuleyan, S.; Lhuillier, E.; Brajuskovic, V.; Guyot-Sionnest, P. Mid-infrared HgTe colloidal quantum dot photodetectors. *Nat. Photonics* **2011**, *5*, 489–493.

[8] Tao, Y. R.; Wu, X. C.; Xiong, W. W. Flexible visible-light photodetectors with broad photoresponse based on ZrS_3 nanobelt films. *Small* **2014**, *10*, 4905–4911.

[9] Tian, W.; Zhang, C.; Zhai, T. Y.; Li, S. L.; Wang, X.; Liu, J. W.; Jie, X.; Liu, D. Q.; Liao, M. Y.; Koide, Y. et al. Flexible ultraviolet photodetectors with broad photoresponse based on branched ZnS-ZnO heterostructure nanofilms. *Adv. Mater.* **2014**, *26*, 3088–3093.

[10] Xie, X. M.; Shen, G. Z. Single-crystalline In_2S_3 nanowire-based flexible visible-light photodetectors with an ultra-high photoresponse. *Nanoscale* **2015**, *7*, 5046–5052.

[11] Li, L.; Wu, P. C.; Fang, X. S.; Zhai, T. Y.; Dai, L.; Liao, M. Y.; Koide, Y.; Wang, H. Q.; Bando, Y.; Golberg, D. Single-crystalline CdS nanobelts for excellent field-emitters and ultrahigh quantum-efficiency photodetectors. *Adv. Mater.* **2010**, *22*, 3161–3165.

[12] Hu, L. F.; Yan, J.; Liao, M. Y.; Xiang, H. J.; Gong, X. G.; Zhang, L. D.; Fang, X. S. An optimized ultraviolet-a light photodetector with wide-range photoresponse based on ZnS/ZnO biaxial nanobelt. *Adv. Mater.* **2012**, *24*, 2305–2309.

[13] Tian, W.; Zhai, T. Y.; Zhang, C.; Li, S. L.; Wang, X.; Liu, F.; Liu, D. Q.; Cai, X. K.; Tsukagoshi, K.; Golberg, D. et al. Low-cost fully transparent ultraviolet photodetectors based on electrospun ZnO-SnO_2 heterojunction nanofibers. *Adv. Mater.* **2013**, *25*, 4625–4630.

[14] Peng, L.; Hu, L. F.; Fang, X. S. Low-dimensional nanostructure ultraviolet photodetectors. *Adv. Mater.* **2013**, *25*, 5321–5328.

[15] Fang, X. S.; Xiong, S. L.; Zhai, T. Y.; Bando, Y.; Liao, M. Y.; Gautam, U. K.; Koide, Y.; Zhang, X. G.; Qian, Y. T.; Golberg, D. High-performance blue/ultraviolet-light-sensitive ZnSe-nanobelt photodetectors. *Adv. Mater.* **2009**, *21*, 5016–5021.

[16] Dan, Y. P.; Seo, K.; Takei, K.; Meza, J. H.; Javey, A.; Crozier, K. B. Dramatic reduction of surface recombination by *in situ* surface passivation of silicon nanowires. *Nano Lett.* **2011**, *11*, 2527–2532.

[17] Lien, D. H.; Retamal, J. R. D.; Ke, J. J.; Kang, C. F.; He, J. H. Surface effects in metal oxide-based nanodevices. *Nanoscale* **2015**, *7*, 19874–19884.

[18] Chen, C. Y.; Retamal, J. R. D.; Wu, I. W.; Lien, D. H.; Chen, M. W.; Ding, Y.; Chueh, Y. L.; Wu, C. I.; He, J. H. Probing surface band bending of surface-engineered metal oxide nanowires. *ACS Nano* **2012**, *6*, 9366–9372.

[19] Dai, X.; Zhang, S.; Wang, Z. L.; Adamo, G.; Liu, H.; Huang, Y. Z.; Couteau, C.; Soci, C. GaAs/AlGaAs nanowire photodetector. *Nano Lett.* **2014**, *14*, 2688–2693.

[20] Li, R. G.; Zhang, F. X.; Wang, D. G.; Yang, J. X.; Li, M. R.; Zhu, J.; Zhou, X.; Han, H. X.; Li, C. Spatial separation of photogenerated electrons and holes among {010} and {110} crystal facets of $BiVO_4$. *Nat. Commun.* **2013**, *4*, 1432.

[21] Zhu, J.; Fan, F. T.; Chen, R. T.; An, H. Y.; Feng, Z. C.; Li, C. Direct imaging of highly anisotropic photogenerated charge separations on different facets of a single $BiVO_4$ photocatalyst. *Angew. Chem., Int. Ed.* **2015**, *54*, 9111–9114.

[22] Yu, J. G.; Low, J. X.; Xiao, W.; Zhou, P.; Jaroniec, M. Enhanced photocatalytic CO_2-reduction activity of anatase TiO_2 by coexposed {001} and {101} facets separations on different facets. *J. Am. Chem. Soc.* **2014**, *136*, 8839–8842.

[23] Roy, N.; Sohn, Y.; Pradhan, D. Synergy of low-energy {101} and high-energy {001} TiO_2 crystal facets for enhanced photocatalysis. *ACS Nano* **2013**, *7*, 2532–2540.

[24] Shen, G. Z.; Liang, B.; Wang, X. F.; Huang, H. T.; Chen, D.; Wang, Z. L. Ultrathin In_2O_3 nanowires with diameters below 4 nm: Synthesis, reversible wettability switching behavior, and transparent thin-film transistor applications. *ACS Nano* **2011**, *5*, 6148–6155.

[25] Shen, G. Z.; Liang, B.; Wang, X. F.; Chen, P. C.; Zhou, C. W. Indium oxide nanospirals made of kinked nanowires. *ACS Nano* **2011**, *5*, 2155–2161.

[26] Shen, G. Z.; Xu, J.; Wang, X. F.; Huang, H. T.; Chen, D. Growth of directly transferable In_2O_3 nanowire mats for transparent thin-film transistor applications. *Adv. Mater.* **2011**, *23*, 771–775.

[27] Huang, S. Y.; Ou, G.; Cheng, J.; Li, H. P.; Pan, W. Ultrasensitive visible light photoresponse and electrical transportation properties of nonstoichiometric indium oxide nanowire arrays by electrospinning. *J. Mater. Chem. C* **2013**, *1*, 6463–6470.

[28] Mottram, A. D.; Lin, Y. H.; Pattanasattayavong, P.; Zhao, K.; Amassian, A.; Anthopoulos, T. D. Quasi two-dimensional dye-sensitized In_2O_3 phototransistors for ultrahigh responsivity and photosensitivity photodetector applications. *ACS Appl. Mater. Interfaces* **2016**, *8*, 4894–4902.

[29] Sun, M.; Xiong, S. J.; Wu, X. L.; He, C. Y.; Li, T. H.; Chu, P. K. Enhanced photocatalytic oxygen evolution by crystal cutting. *Adv. Mater.* **2013**, *25*, 2035–2039.

[30] Meng, M.; Wu, X. L.; Zhu, X. B.; Yang, L.; Gan, Z. X.; Zhu, X. S.; Liu, L. Z.; Chu, P. K. Cubic In_2O_3 microparticles for efficient photoelectrochemical oxygen evolution. *J. Phys. Chem. Lett.* **2014**, *5*, 4298–4304.

[31] Meng, M.; Wu, X. L.; Zhu, X. B.; Zhu, X. S.; Chu, P. K. Facet cutting and hydrogenation of In_2O_3 nanowires for enhanced photoelectrochemical water splitting. *ACS Appl. Mater. Interfaces* **2014**, *6*, 4081–4088.

[32] Hu, L. F.; Yan, J.; Liao, M. Y.; Wu, L. M.; Fang, X. S. Ultrahigh external quantum efficiency from thin SnO_2 nanowire ultraviolet photodetectors. *Small* **2011**, *7*, 1012–1017.

[33] Lu, J. F.; Xu, C. X.; Dai, J.; Li, J. T.; Wang, Y. Y.; Lin, Y.; Li, P. L. Improved UV photoresponse of ZnO nanorod arrays by resonant coupling with surface plasmons of Al nanoparticles. *Nanoscale* **2015**, *7*, 3396–3403.

[34] Shao, D. L.; Qin, L. Q.; Sawyer, S. Near ultraviolet photodetector fabricated from polyvinyl-alcohol coated In_2O_3 nanoparticles. *Appl. Surf. Sci.* **2012**, *261*, 123–127.

[35] Chong, H. N.; Wei, G. D.; Hou, H. L.; Yang, H. J.; Shang, M. H.; Gao, F. M.; Yang, W. Y.; Shen, G. Z. High-performance solar-blind ultraviolet photodetector based on electrospun TiO_2-$ZnTiO_3$ heterojunction nanowires. *Nano Res.* **2015**, *8*, 2822–2832.

[36] Zou, R. J.; Zhang, Z. Y.; Liu, Q.; Hu, J. Q.; Sang, L. W.; Liao, M. Y.; Zhang, W. J. High detectivity solar-blind high-temperature deep-ultraviolet photodetector based on multi-layered (l00) facet-oriented β-Ga_2O_3 nanobelts. *Small* **2014**, *10*, 1848–1856.

[37] Wang, R.; Hashimoto, K.; Fujishima, A.; Chikuni, M.; Kojima. E.; Kitamura, A.; Shimohigoshi, M.; Watanabe, T. Light-induced amphiphilic surfaces. *Nature* **1997**, *388*, 431–432.

[38] Lim, H. S.; Kwak, D.; Lee, D. Y.; Lee, S. G.; Cho, K. UV-driven reversible switching of a roselike vanadium oxide film between superhydrophobicity and superhydrophilicity. *J. Am. Chem. Soc.* **2007**, *129*, 4128–4129.

[39] Feng, X. J.; Feng, L.; Jin, M. H.; Zhai, J.; Jiang, L.; Zhu, D. B. Reversible super-hydrophobicity to super-hydrophilicity transition of aligned ZnO nanorod films. *J. Am. Chem. Soc.* **2004**, *126*, 62–63.

[40] Adler-Abramovich, L.; Aronov, D.; Beker, P.; Yevnin, M.; Stempler, S.; Buzhansky, L.; Rosenman, G.; Gazit, E. Self-assembled arrays of peptide nanotubes by vapour deposition. *Nat. Nanotechnol.* **2009**, *4*, 849–854.

[41] Miyauchi, M.; Nakajima, A.; Watanabe, T.; Hashimoto, K. Photocatalysis and photoinduced hydrophilicity of various metal oxide thin films. *Chem. Mater.* **2002**, *14*, 2812–2816.

[42] Yadav, K.; Mehta, B. R.; Singh, J. P. Superhydrophobicity and enhanced UV stability in vertically standing indium oxide nanorods. *Appl. Surf. Sci.* **2015**, *346*, 361–365.

[43] Zhu, W. Q.; Feng, X. J.; Feng, L.; Jiang, L. UV-manipulated wettability between superhydrophobicity and superhydrophilicity on a transparent and conductive SnO_2 nanorod film. *Chem. Commun.* **2006**, 2753–2755.

[44] Zhong, M.; Zheng, M. J.; Zeng, A. S.; Ma, L. Direct integration of vertical In_2O_3 nanowire arrays, nanosheet chains, and photoinduced reversible switching of wettability. *Appl. Phys. Lett.* **2008**, *92*, 093118.

Electronic Supplementary Material

Ultrahigh quantum efficiency photodetector and ultrafast reversible surface wettability transition of square In_2O_3 nanowires

Ming Meng[1,2], Xinglong Wu[2] (✉), Xiaoli Ji[3], Zhixing Gan[4], Lizhe Liu[2], Jiancang Shen[2], and Paul K. Chu[5]

[1] *School of Physics and Telecommunication Engineering, Zhoukou Normal University, Zhoukou 466001, China*
[2] *Key Laboratory of Modern Acoustics, MOE, Institute of Acoustics, Collaborative Innovation Center of Advanced Microstructures, National Laboratory of Solid State Microstructures, Nanjing University, Nanjing 210093, China*
[3] *School of Electronic Science and Engineering, Nanjing University, Nanjing 210093, China*
[4] *Key Laboratory of Optoelectronic Technology of Jiangsu Province, School of Physical Science and Technology, Nanjing Normal University, Nanjing 210023, China*
[5] *Department of Physics and Materials Science, City University of Hong Kong, Tat Chee Avenue, Kowloon, Hong Kong, China*

Supporting information to DOI 10.1007/s12274-017-1481-y

Table S1 Rise time, decay time, spectral responsivity (R_λ), and external quantum efficiency (EQE) of the photodetector after 20 periodic change

Rsie time	Decay time	R_λ	EQE
3 s	13 s	4.75×10^6 (A/W)	1.45×10^7

Table S2 Comparison of the response speeds from the present In_2O_3-based photodetector and previously reported In_2O_3 based photodetectors

Photodetector	Rsie time	Decay time	Reference
In_2O_3 nanowires	15 s	100 s	[S1]
In_2O_3 nanoparticles	500 s	1,600 s	[S2]
In_2O_3 nanowires	3 s	13 s	This work

Address correspondence to hkxlwu@nju.edu.cn

Table S3 Comparison of EQE and R_λ from this work and previous reports

Photodetector	EQE	R_λ	Dark current	Photocurrent	Reference
In_2O_3 nanoparticles	—	2×10^3 (A/W)	—	—	[S3]
In_2S_3 nanowire	2.28×10^5	7.35×10^4 (A/W)	0.12 pA (at 5 V)	293 nA (at 5 V)	[S4]
CdS nanobelt	1.9×10^5	7.3×10^4 (A/W)	5 μA (at 1 V)	30 μA (at 1 V)	[S5]
ZnS/ZnO biaxial nanobelt	2×10^6	5×10^5 (A/W)	0.67 μA (at 1 V)	4.64 μA (at 1 V)	[S6]
SnO_2 nanowire	1.32×10^7	—	19.4 nA (at 1 V)	2.1 μA (at 1 V)	[S7]
Ga_2O_3 nanobelt	4.2×10^3	851 (A/W)	—	—	[S8]
In_2O_3 nanowire	1.46×10^7	4.8×10^6 (A/W)	0.45 μA (at 5 V)	21.7 μA (at 5 V)	This work

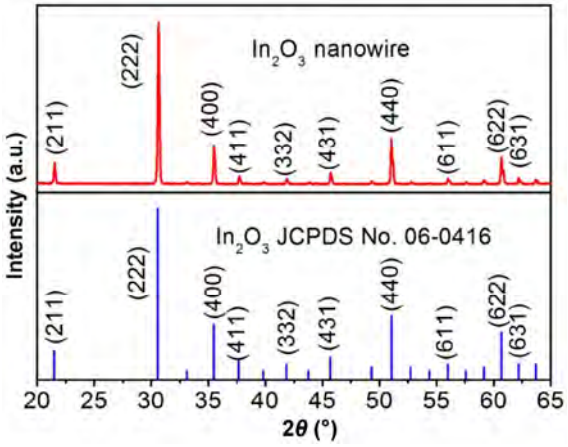

Figure S1 XRD patterns acquired from the square In_2O_3 NWs. All the diffraction peaks match those of the bcc structure of In_2O_3 (JCPDS card No. 06-0416).

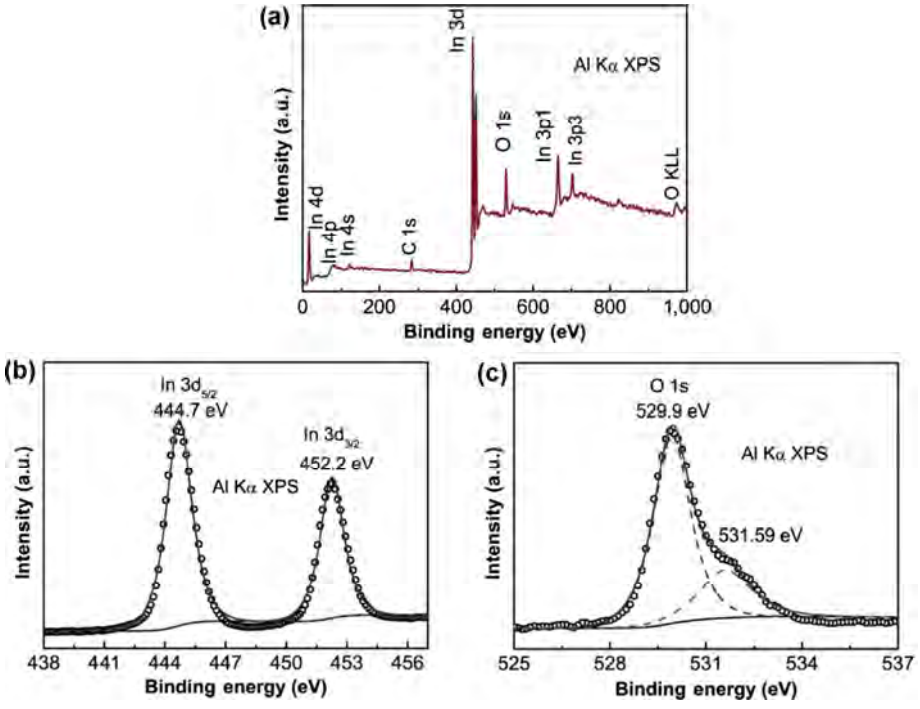

Figure S2 (a) Wide-scan survey XPS spectrum for In_2O_3 NWs. (b) and (c) High-resolution XPS spectra of In 3d and O 1s obtained from the In_2O_3 NWs, respectively.

The wide-scan survey XPS spectrum shows the presence of only In, O, and C in the square In_2O_3 NWs, suggesting that they have a pure In_2O_3 phase (Fig. S2(a)). Figure S2(b) is the high-resolution XPS spectrum of In 3d showing characteristic peaks of 447.7 eV (In $3d_{5/2}$) and 452.2 eV (In $3d_{3/2}$) corresponding to chemical element state of In^{3+} (In_2O_3). In the O 1s spectrum, the peak at 529.9 eV and shoulder at 531.6 eV are observed. The peak at 529.9 eV is ascribed to the oxygen bond of In–O–In, whereas that at 531.6 eV is attributed to surface oxygen defects. The analytical results confirm that the NWs are pure In_2O_3 with some oxygen defects.

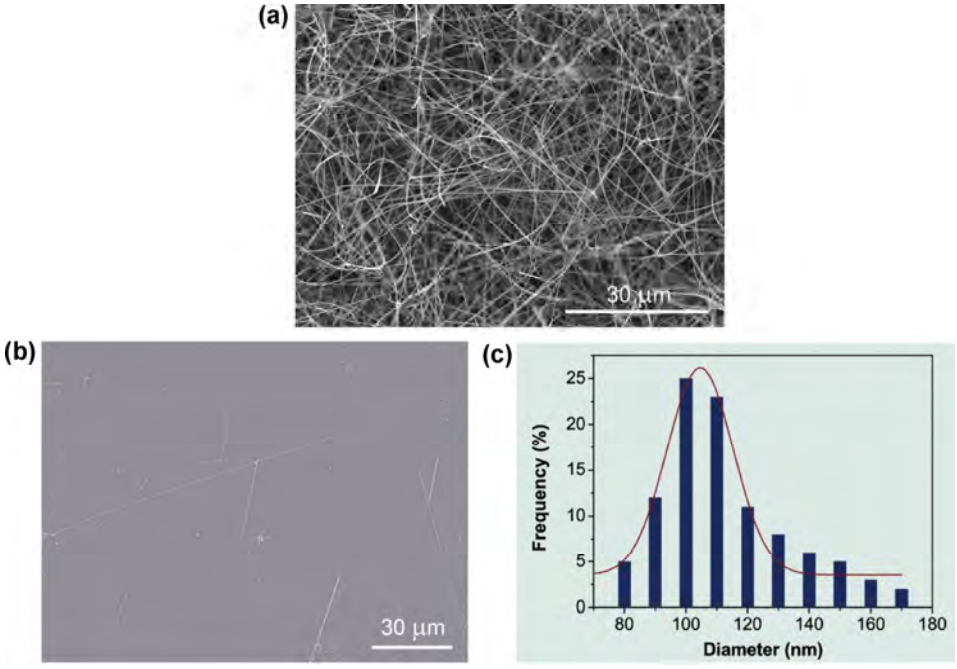

Figure S3 (a) and (b) Low-magnification FE-SEM images of the In_2O_3 NWs fabricated on an Au-coated Si substrate and a thermally oxidized Si substrate covered with a 300 nm SiO_2 layer with a sparse density, respectively, revealing that the NWs are several tens to hundreds of micrometers in length. (c) NWs diameter distribution showing that the main distribution diameter of the NWs is around 100 nm.

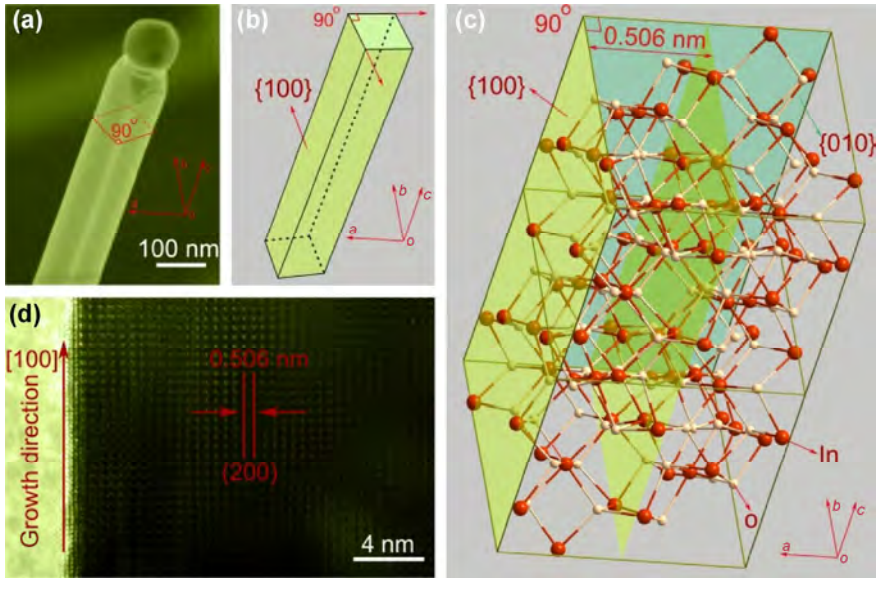

Figure S4 (a) High-magnification FE-SEM image of an In_2O_3 NW displaying the perfect square cross section. (b) Schematic diagram of an In_2O_3 NW. The four side facets are {001} facets. (c) Schematic model of an ideal In_2O_3 NW enclosed by the {001} facets. (d) HR-TEM image of the In_2O_3 NW.

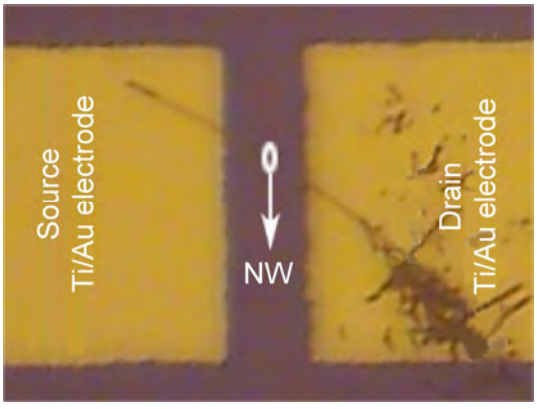

Figure S5 Optical microscope image of the whole photodetector device clearly demonstrating that there is only one NW between source and drain.

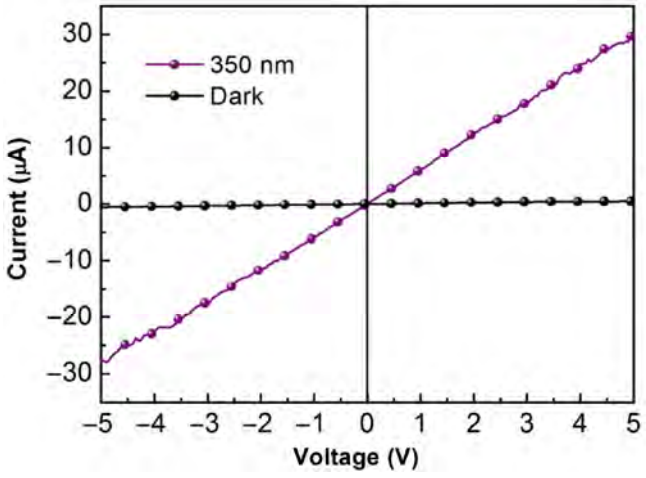

Figure S6 *I–V* curves of device 1 illuminated with 350 nm light (1.6 mW/cm^2) and under dark conditions.

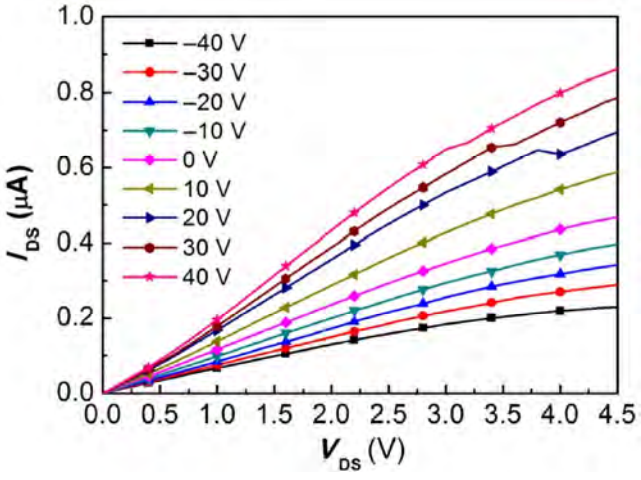

Figure S7 Drain current vs. drain voltage (I_{ds}–V_{ds}) curves recorded from a single In_2O_3 NW-based FETs with the gate voltage from 40 to –40 V. The I_{ds}–V_{ds} curve is nearly linear, suggesting good Ohmic contact between the NW and electrodes.

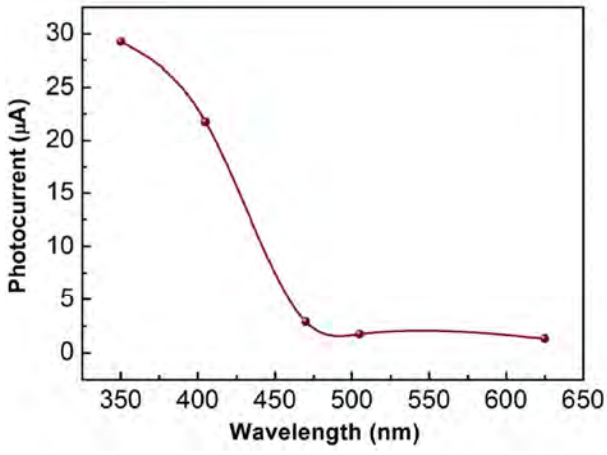

Figure S8 Comparison of the photocurrents obtained at 5 V from device 1.

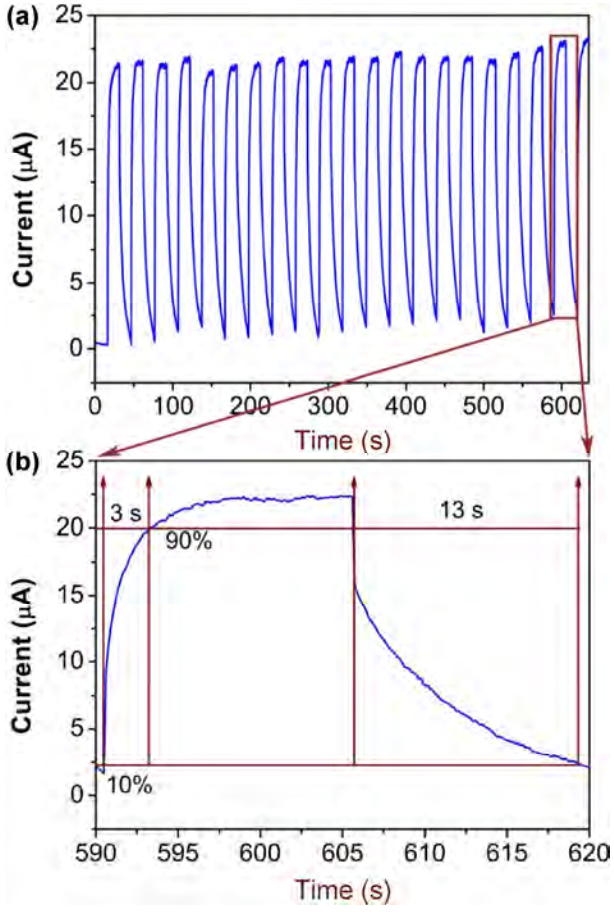

Figure S9 (a) Current–time response measured by periodically switching on and off 405 nm light illumination at a bias of 5 V, showing the long-term stability of the In_2O_3 NW-based photodetector. (b) Enlargement of the curve in the 590–620 s range outlined in (a).

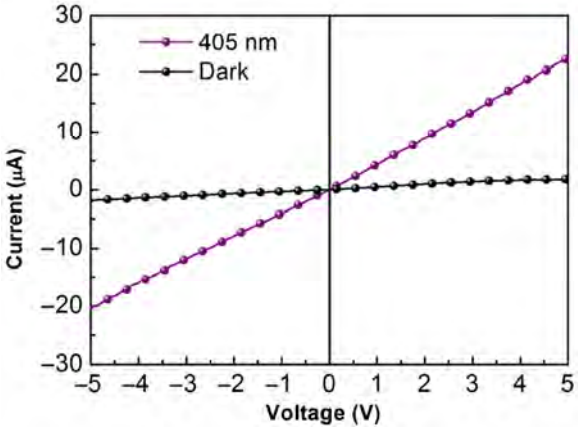

Figure S10 *I–V* curves of device 1 illuminated with the 405 nm light (1.21 mW/cm^2) and under dark conditions after 20 periodic switching. Based on this figure, R_λ and EQE of the NW-based photodetector can be calculated and the results are shown in Table S1.

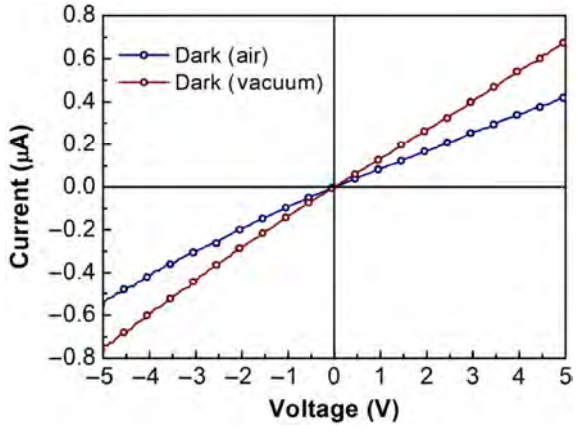

Figure S11 *I–V* curves of the NW-based photodetector without illumination in air and under vacuum conditions.

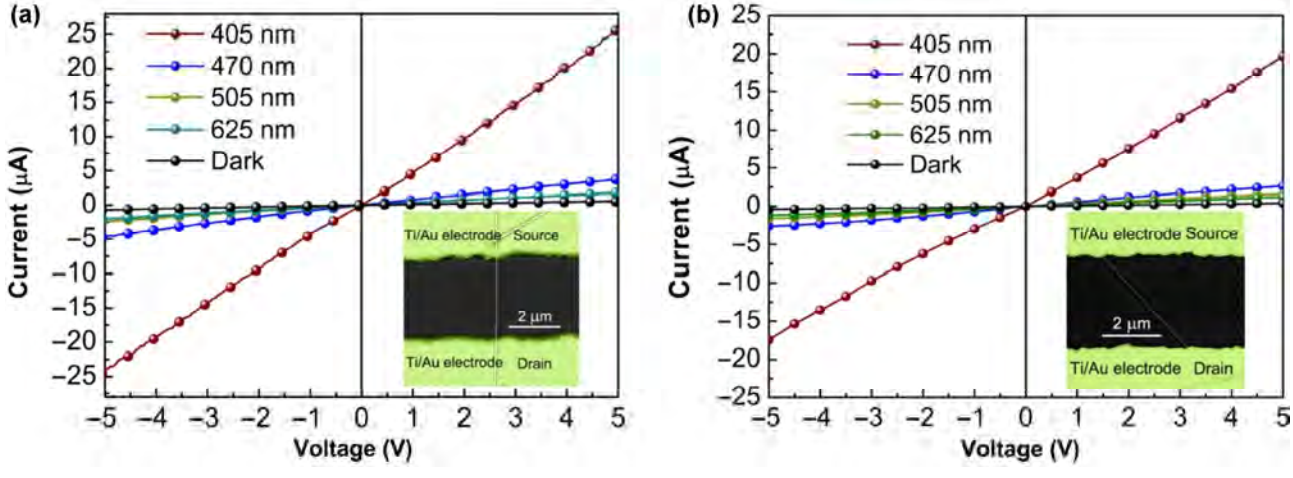

Figure S12 (a) *I–V* curves of device 2 illuminated with the 405, 470, 505, and 625 nm light, and under dark conditions. Inset is the SEM image of device 2 with a channel width of 3 μm between two electrodes. (b) *I–V* curves of device 3 obtained under the same test conditions as for device 2. Inset is the SEM image of device 3 with a channel width of 4 μm between two electrodes.

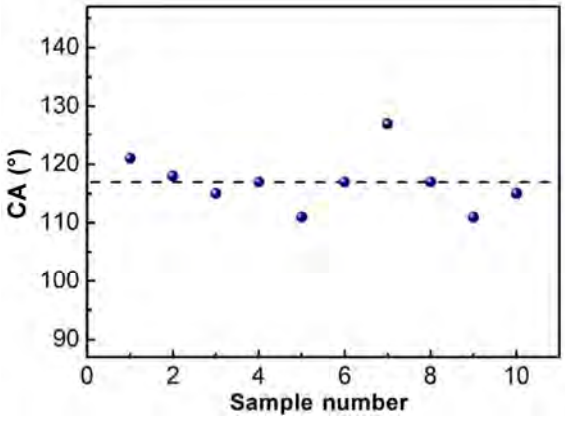

Figure S13 Contact angles measured from different In_2O_3 samples, demonstrating the hydrophobic properties of the In_2O_3 NWs with average contact angle of about 120°.

References

[S1] Huang, S. Y.; Ou, G.; Cheng, J.; Li, H. P.; Pan, W. Ultrasensitive visible light photoresponse and electrical transportation properties of nonstoichiometric indium oxide nanowire arrays by electrospinning. *J. Mater. Chem. C* **2013**, *1*, 6463–6470.

[S2] Shao, D. L.; Qin, L. Q.; Sawyer, S. Near ultraviolet photodetector fabricated from polyvinyl-alcohol coated In_2O_3 nanoparticles. *Appl. Surf. Sci.* **2012**, *261*, 123–127.

[S3] Mottram, A. D.; Lin, Y. H.; Pattanasattayavong, P.; Zhao, K.; Amassian, A.; Anthopoulos, T. D. Quasi two-dimensional dye-sensitized In_2O_3 phototransistors for ultrahigh responsivity and photosensitivity photodetector applications. *ACS Appl. Mater. Interfaces* **2016**, *8*, 4894–4902.

[S4] Xie, X. M.; Shen, G. Z. Single-crystalline In_2S_3 nanowire-based flexible visible-light photodetectors with an ultra-high photoresponse. *Nanoscale* **2015**, *7*, 5046–5052.

[S5] Li, L.; Wu, P. C.; Fang, X. S.; Zhai, T. Y.; Dai, L.; Liao, M. Y.; Koide, Y.; Wang, H. Q.; Bando, Y.; Golberg, D. Single-crystalline CdS nanobelts for excellent field-emitters and ultrahigh quantum-efficiency photodetectors. *Adv. Mater.* **2010**, *22*, 3161–3165.

[S6] Hu, L. F.; Yan, J.; Liao, M. Y.; Xiang, H. J.; Gong, X. G.; Zhang, L. D.; Fang, X. S. An optimized ultraviolet—A light photodetector with wide-range photoresponse based on ZnS/ZnO biaxial nanobelt. *Adv. Mater.* **2012**, *24*, 2305–2309.

[S7] Hu, L. F.; Yan, J.; Liao, M. Y.; Wu, L. M.; Fang, X. S. Ultrahigh external quantum efficiency from thin SnO_2 nanowire ultraviolet photodetectors. *Small* **2011**, *7*, 1012–1017.

[S8] Zou, R. J.; Zhang, Z. Y.; Liu, Q.; Hu, J. Q.; Sang, L. W.; Liao, M. Y.; Zhang, W. J. High detectivity solar-blind high-temperature deep-ultraviolet photodetector based on multi-layered (l00) facet-oriented β-Ga_2O_3 nanobelts. *Small* **2014**, *10*, 1848–1856.